



Research paper

Experimental investigation of modified desulfurized gypsum-based concrete permeability performance

Yong Luo¹, Shuai Ren², Diancai Xiao³, Cong Gao⁴,
Linfeng Xu⁵, Hao Wu⁶

Abstract: To comprehend the permeability behavior of modified desulfurized gypsum-based concrete under varying stress conditions, this investigation conducted permeability assessments under both confining pressure and unloading circumstances. The findings suggest that an escalation in confining pressure results in a reduction in the specimen permeability. Conversely, a decrease in confining pressure leads to a gradual increment in permeability, albeit without fully reverting to its initial state. The rise in pore water pressure diminishes the effective confining pressure experienced by the specimen, thereby enhancing the interconnectivity of the internal pore structure and facilitating an increase in permeability. As the confining pressure intensifies, the volumetric strain also increases. Conversely, a reduction in confining pressure corresponds to a decrease in volumetric strain, though it does not return to its initial level. This observation implies that solely the elastic deformation of the specimen can recover as the confining pressure decreases. The internal pore structure distribution of modified desulfurized gypsum-based concrete is predominantly characterized by micropores, with a permeability coefficient in the order of magnitude of 10^{-17} m², contributing to its commendable impermeability.

Keywords: desulfurization gypsum, underground engineering, concrete, permeability, confining pressure

¹Eng., State Key Laboratory of Deep Coal Mining & Environment Protection, Huainan Mining (Group) Co., Ltd., Huainan 232001, China, e-mail: yongluo2023@163.com, ORCID: 0009-0008-1259-0163

²Eng., Ping'an Coal Mining Engineering Technology Research Institute Co., Ltd., Huainan 232001, China, e-mail: renshuai202310@163.com, ORCID: 0009-0002-1422-1691

³Ping'an Coal Mining Engineering Technology Research Institute Co., Ltd., Huainan 232001, China, e-mail: xiaodiancai2023@163.com, ORCID: 0009-0007-0976-329X

⁴MSc., Eng., School of Civil Engineering and Architecture, Anhui University of Science and Technology, Huainan 232001, China, e-mail: 2020200267@aust.edu.cn, ORCID: 0000-0001-8718-5746

⁵MSc., School of Civil Engineering and Architecture, Anhui University of Science and Technology, Huainan 232001, China, e-mail: 2021200521@aust.edu.cn, ORCID: 0000-0002-0841-8837

⁶MSc., School of Civil Engineering and Architecture, Anhui University of Science and Technology, Huainan 232001, China, e-mail: hwu@aust.edu.cn, ORCID: 0009-0001-2139-7006

1. Introduction

As human society reaches unprecedented levels of development, the demand for energy continues to surge. Despite ongoing advancements in the exploration and deployment of alternative energy sources, coal remains at the helm of the power generation hierarchy [1]. In the process of coal combustion, the release of sulfur dioxide (SO_2) is a common occurrence. Presently employed flue gas desulfurization techniques have managed to curtail SO_2 emissions, albeit at the cost of generating substantial volumes of recalcitrant solid waste. Desulfurized gypsum, a quintessential example, emerges as a byproduct of this process.

In the pursuit of harnessing industrial solid waste to produce cementitious materials and address ecological environmental concerns, Wang et al. [2] embarked on a groundbreaking exploration of the synergistic effects of desulfurized gypsum, red mud, and fly ash in cementitious materials. Their work not only offered a novel avenue for handling solid waste and desulfurized gypsum but also provided a comprehensive analysis of the microscopic and macroscopic mechanical properties of desulfurized gypsum's impact on cementitious materials. Furthermore, Gao et al. [3] utilizing varying proportions of desulfurized gypsum (ranging from 1.6% to 2.8%), delved into the influence of desulfurized gypsum on the strength of fly ash-based polymers, revealing that an appropriate proportion of desulfurized gypsum can augment the concrete's strength. Additionally, Liu et al. [4] delved into the temporal performance when incorporating desulfurized gypsum into cementitious materials, noting that the presence of desulfurized gypsum spurred the formation of ettringite in the early-age concrete, thus endowing it with higher initial strength. Scholars have been actively seeking novel outlets for solid waste desulfurized gypsum. They are either researching its effects on the performance of cementitious materials when incorporated, or considering the synergistic interaction of desulfurized gypsum with other solid wastes. The studies have substantiated the feasibility of desulfurized gypsum in enhancing the performance of cementitious materials.

However, throughout this process, desulfurized gypsum has primarily served as an additive or has been incorporated in minute quantities. Consequently, the consumption of desulfurized gypsum remains significantly below its production volume, necessitating a more profound exploration of its potential applications. Tan et al. [5] for instance, conducted tests involving the replacement of 0%, 10%, 15%, 20%, 25%, and 30% of cement with desulfurized gypsum in concrete specimens. Their research revealed that the compressive strength of the 28-day cured samples met the C30 concrete strength standards. Moreover, Shi et al. [6] went a step further by exploring the mechanical performance differences between modified desulfurized gypsum-based concrete and cement-based concrete at various ages. Their experiments demonstrated that the mechanical properties of modified desulfurized gypsum-based concrete closely approximated those of cement-based concrete. Both studies experimented with a substantial proportion of desulfurized gypsum replacing cement as the binding material, providing evidence of the potential for desulfurized gypsum to further substitute cement. However, these investigations did not consider the intricate environmental conditions encountered in practical engineering applications. Today, the demand for concrete materials in underground engineering lining and support structures is progressively on the rise [7]. Additionally, the structural requirements for support materials under such conditions are relatively modest,

necessitating strengths of merely 20–25 MPa. Nevertheless, there are stringent requirements concerning permeability, and the permeability performance may vary in different sections of the underground environment, where varying stress conditions and groundwater pressures are at play. Therefore, for engineering endeavors deep beneath the earth's surface, such as mines and tunnels extending to hundreds or even thousands of meters underground, it becomes imperative to consider the influence of in-situ stress and groundwater pressure on the utilization of lining support structures [8].

This study focused on modifying desulfurization gypsum (FGD) gypsum to create modified FGD gypsum-based concrete, aiming to transform FGD gypsum, a solid waste material, into a valuable cementitious substance. Employing a rock servo triaxial testing apparatus to exert confining pressure and pore water pressure, the study delved into the progression of permeability within modified desulfurized gypsum-based concrete under triaxial stress conditions. Furthermore, it scrutinized the deformation attributes of specimens amidst changes in confining pressure and conducted an exhaustive analysis of the concrete's microscopic pore structure. The permeability characteristics of modified desulfurized gypsum-based concrete and its evolution pattern under varying stress conditions have been elucidated, shedding light on the internal pore structure matrix of modified desulfurized gypsum-based concrete, thereby facilitating a comprehensive assessment of its resistance to seepage. The findings of this study furnish both experimental and theoretical groundwork for the application of modified desulfurized gypsum-based concrete as a material for lining support in underground engineering projects.

2. Experimental schemes

2.1. Raw materials and specimen preparation

This experiment utilized crushed stone with a particle size ranging from 5 to 15 millimeters and bearing a fragmentation index of 9.8% as the coarse aggregate. A fine aggregate of a fineness modulus of 2.68, referred to as medium sand, was employed. The modification of desulfurized gypsum was achieved through the incorporation of cement, slag, fly ash, and various additives. This modified desulfurized gypsum was intended to serve as a cementitious material. The formulation was designed with a mass ratio of gypsum, fly ash, slag, and cement set at 4:1:2:3, with additives as follows: superplasticizer dosage of 1%, redispersible latex powder dosage of 0.1%, defoaming agent dosage of 0.1%, retarding agent dosage of 0.1%, dodecahydrate potassium aluminum sulfate dosage of 0.15%, and cellulose ether dosage of 0.01%. As per the specifications outlined in Table 1, cylindrical specimens with dimensions $\varphi 50 \text{ mm} \times 100 \text{ mm}$ were prepared for permeability testing. Furthermore, standard cubic specimens measuring $150 \text{ mm} \times 150 \text{ mm} \times 150 \text{ mm}$ were cast for measuring the compressive strength of the modified desulfurized gypsum-based concrete. The compressive strength of the modified desulfurized gypsum-based concrete was determined to be 29.7 MPa.

Table 1. Test mix ratio

W/C	Percentage of sand	Concrete material consumption (kg/m ³)							
		Modified desulfurization gypsum					Pebble	Sand	Water
0.4	50%	Desulfurization gypsum	Fly ash	Slag	Cement	Admixture	888.9	888.9	177.8
		177.76	44.44	88.88	133.32				

The modified desulfurized gypsum-based concrete, which has undergone a 28-day curing process, was subjected to X-ray Diffraction (XRD) analysis. The XRD analysis results are depicted in Fig. 1.

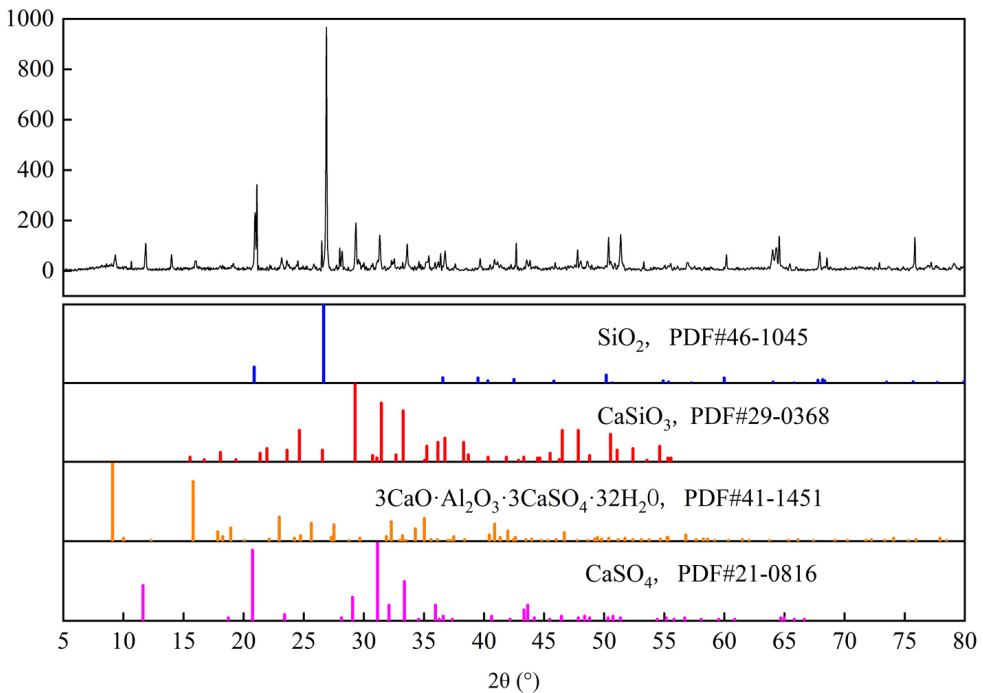


Fig. 1. XRD analysis of modified desulfurization gypsum-based concrete

2.2. Equipment and test methods

The permeability assessment of modified desulfurized gypsum-based concrete was conducted under varying confining pressures and water pressures utilizing the TAW-2000 electro-hydraulic servo triaxial testing machine. The experimental setup was computerized to regulate three key parameters: axial load, confining pressure, and pore water pressure. Furthermore, strain gauges were incorporated to facilitate the measurement of axial and radial deformation

of the specimens. The pore water pressures were established at 0.25 MPa, 0.5 MPa, 1 MPa, 2 MPa, 3 MPa, and 4 MPa for the six test sets. The schematic depiction of the seepage principle is illustrated in Fig. 2.

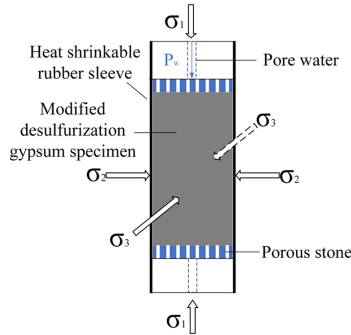


Fig. 2. Triaxial permeability of modified desulfurization gypsum-based concrete

Before commencing the experiment, the modified desulfurized gypsum-based concrete specimens underwent thorough saturation using a vacuum saturation apparatus [9]. These fully saturated specimens were then positioned within the triaxial chamber. To secure their placement, an axial load of 1 kN was applied at a displacement loading rate of 1 mm/min. Subsequently, instructions were given to initiate the initial confining pressure of 5 MPa. Once the designated confining pressure was achieved, directives for the predetermined pore water pressure values were communicated. Data collection commenced 30 minutes post the onset of seepage, and a continuous monitoring of the water flow rate versus time curve was initiated. The pore water pressure remained constant throughout the loading process. Upon stabilization of the slope of the water flow rate versus time curve, the confining pressure was adjusted following the sequence of 5 MPa \rightarrow 7 MPa \rightarrow 10 MPa \rightarrow 14 MPa \rightarrow 19 MPa \rightarrow 25 MPa \rightarrow 30 MPa \rightarrow 25 MPa \rightarrow 19 MPa \rightarrow 14 MPa \rightarrow 10 MPa \rightarrow 7 MPa \rightarrow 5 MPa, in a cyclic loading and unloading manner. Throughout the entire seepage process, the computer system automatically recorded data related to water flow, deformation, and stress. By applying Darcy's law [10], the permeability of the modified desulfurized gypsum-based concrete specimens under various stress conditions was calculated in accordance with Eq. (2.1).

$$(2.1) \quad K = \frac{\mu L \Delta_Q}{A P \Delta_t}$$

where: K – represents the permeability of specimen (m^2), L – represents the height of specimen (m), Δ_Q – represents the seepage flow volume within Δ_t time (m^3), μ – represents the viscosity coefficient of the seepage fluid (typically 1.005×10^{-3} Pa·s at room temperature), A – represents the seepage area (m^2), P – represents the pressure difference driving the seepage (Pa).

3. Results and discussion

3.1. The evolution of permeability behavior

Fig. 3 illustrates the experimental data showing the variation of permeability with changes in confining pressure during different pore water pressures. As depicted in Fig. 3, it is evident that the permeability exhibits a marked decrease during the confining pressure loading process. In the initial stages of confining pressure loading, the compression effect of the confining pressure reduces the pore size [11], here referring to micropores and microcracks, resulting in a rapid decrease in permeability. As the confining pressure continues to increase, the rate of permeability reduction gradually diminishes. This phenomenon arises because the number of internal pores that can be further compacted decreases as the confining pressure increases, reaching a limit beyond which it no longer changes. Consequently, the entire permeability versus confining pressure curve exhibits pronounced nonlinear characteristics.

Under the same pore water pressure, the reduction in specimen permeability exhibits distinct characteristics at confining pressures of approximately 10 MPa (designated as point “a”) and 19 MPa (designated as point “b”). When the confining pressure is less than 10 MPa, the permeability decreases rapidly. As the confining pressure exceeds 10 MPa but remains below 19 MPa, the rate of permeability reduction becomes less steep. Beyond 19 MPa, the permeability approaches a plateau. This behavior can be attributed to the early stages of confining pressure loading, during which a significant number of seepage channels are compacted, resulting in a reduction in their inner diameter. With further increases in confining pressure, most of the narrower inner diameter seepage channels become fully compacted, and even the wider inner diameter channels begin to constrict under the influence of the confining pressure. This gradual constriction leads to a reduced rate of permeability reduction. Upon reaching point “b”, the internal porosity within the specimen, subjected to the confining pressure, is nearly minimized and cannot be further compressed, effectively causing most seepage channels to be fully compacted [12]. Therefore, even if the confining pressure continues to rise, the permeability will remain relatively stable and undergo minimal change.

During the unloading process, the permeability of the specimen demonstrates varying degrees of recovery. It is noteworthy that under the same confining pressure, the permeability during unloading is notably less than that observed during the loading process. As the confining pressure decreases, the extent of permeability recovery diminishes, and the magnitude of recovery falls far short of the permeability values observed during loading. Characteristic point “c” in the permeability recovery during unloading is reached at approximately 14 MPa of confining pressure. When unloading the confining pressure to 25 MPa, 19 MPa, and 14 MPa, the permeability under the same pore water pressure remains nearly identical, indicating that the unloading of confining pressure has minimal impact on permeability at this stage. However, when unloading the confining pressure to 10 MPa, 7 MPa, and 5 MPa, the permeability under the same pore water pressure begins to increase as the confining pressure decreases. Nevertheless, the recovery of permeability becomes more pronounced at lower confining pressures, particularly when unloading to lower confining pressures, as a portion of the seepage channels that underwent plastic deformation during the loading process cannot recover during

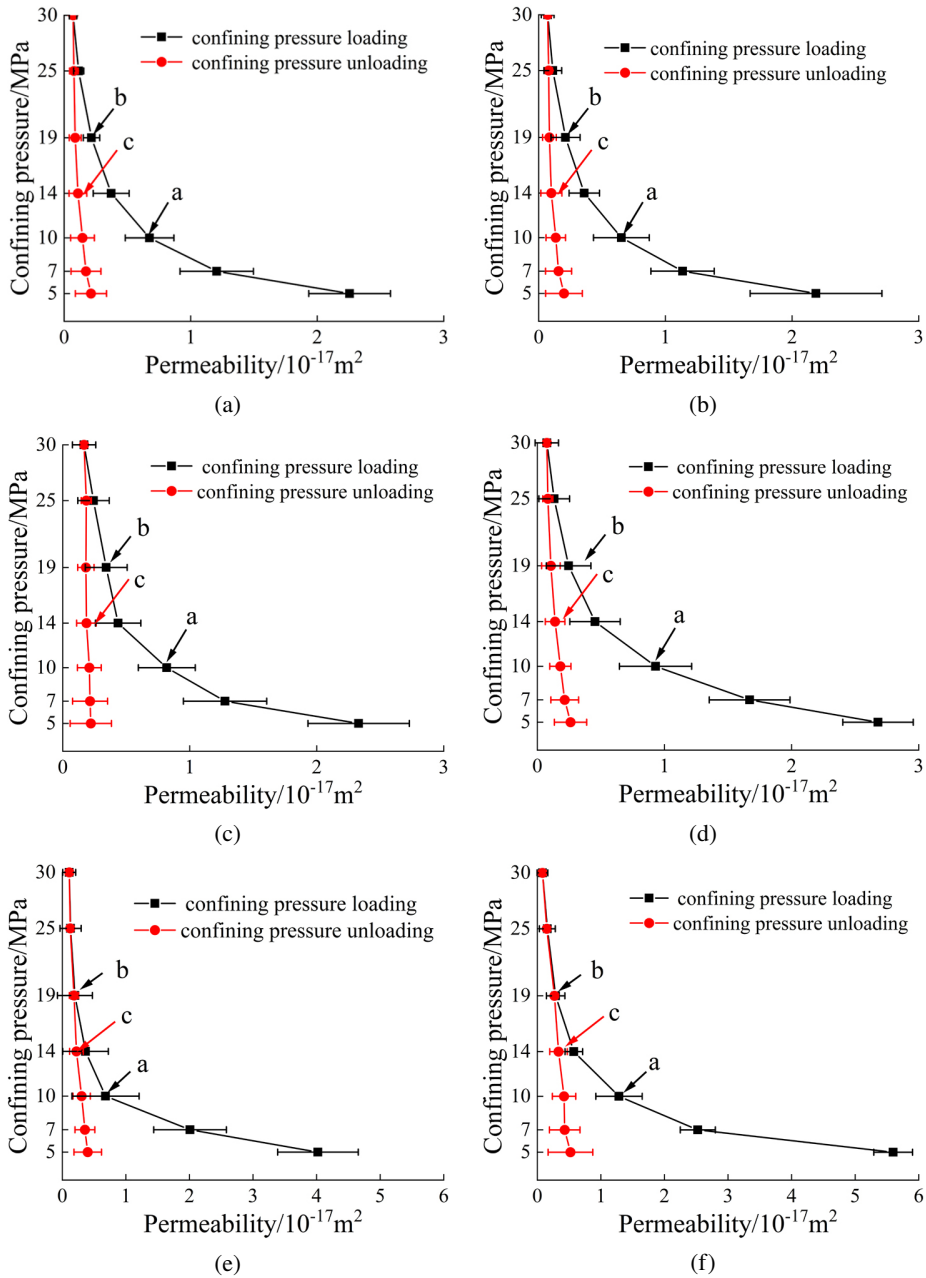


Fig. 3. Permeability and confining pressure curve. Pore water pressure: (a) 0.25 MPa, (b) 0.5 MPa, (c) 1 MPa, (d) 2 MPa, (e) 3 MPa, (f) 4 MPa

compression and dissipates energy in the form of internal energy [13]. Consequently, some permeability recovery occurs with decreasing confining pressure, which, on a macroscopic level, manifests as a loss in permeability.

To further analyze the permeability evolution under different pore water pressures, the graph in Fig. 4 depicts the variation of permeability with changing confining pressure. From Fig. 4, it is evident that as pore water pressure increases, permeability exhibits a growing trend. Even at the same confining pressure, different pore water pressure values result in varying permeabilities. However, the differences in permeability values remain within a relatively narrow range and do not exhibit significant orders of magnitude disparity. For instance, when the confining pressure is 5 MPa, and the pore water pressure varies between 0.25 MPa, 0.5 MPa, 1 MPa, 2 MPa, 3 MPa, and 4 MPa, the initial permeabilities of the specimens are respectively as follows: $2.19 \times 10^{-17} \text{ m}^2$, $2.26 \times 10^{-17} \text{ m}^2$, $2.33 \times 10^{-17} \text{ m}^2$, $2.68 \times 10^{-17} \text{ m}^2$, $4.02 \times 10^{-17} \text{ m}^2$, and $5.59 \times 10^{-17} \text{ m}^2$. Several factors contribute to these observations. Firstly, there is interaction between pore water pressure and confining pressure, necessitating consideration of the actual influence of effective stress [14]. Secondly, hydraulic pressure affects the internal pore structure of the specimens. The scouring effect of pore water pressure and its expansion may weaken the crystalline products within the cementitious matrix and even lead to the detachment of weakly bonded particles. These fragments, under stress, dissolve and migrate, exerting a splitting effect on unconnected cracks, accelerating microcrack propagation, and altering the internal pore structure of the specimen. As pore water pressure increases, the internal pore structure of the specimen experiences greater stress, amplifying the impact of seepage on the internal pore structure. Consequently, with rising pore water pressure, the seepage channels further expand, reflecting a macroscopic trend where permeability increases with the gradual rise in pore water pressure.

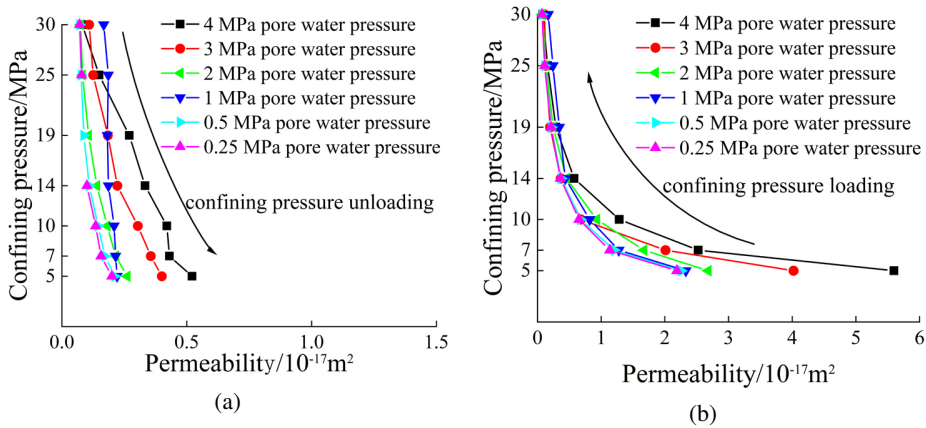


Fig. 4. Variation curves of permeability: (a) Process of confining pressure loading, (b) Process of confining pressure unloading

As the confining pressure increases from 5 MPa to 30 MPa, corresponding to pore water pressures ranging from 0.25 MPa to 4 MPa, the specimen permeability experiences growth by the following percentages: 155.69%, 122.18%, 96.78%, 59.44%, 36.29%, 41.33%, and 15.09%.

It is noticeable that during the lower confining pressure stages, variations in pore water pressure have a more significant impact on permeability [15]. However, when the confining pressure reaches 30 MPa, the influence of pore water pressure on permeability diminishes, with a growth rate of only 15.09%, significantly lower than the growth rate observed under lower confining pressures. This can be attributed to the increased confining pressure, which compresses and closes internal tensile cracks within the specimen, leading to increased resistance for pore water to penetrate the interior of microcracks. Consequently, this reduces the damaging effect of pore water pressure on the internal structure of the specimen.

3.2. The evolution of volumetric strain during seepage process

During the seepage testing process, an extensometer was used to monitor the axial and radial deformations of the specimen during the confining pressure loading and unloading phases. The deformation at 5 MPa of confining pressure was taken as the initial value, and the strain variations during the confining pressure loading and unloading were recorded. By observing the pattern of strain changes, the deformation characteristics of the confining pressure loading and unloading were determined, allowing for an analysis of the mechanism of permeability variation with respect to confining pressure. The volumetric strain of the specimen during the loading and unloading phases were calculated according to Eq. (3.1). The curve of strain variation with confining pressure is shown in Fig. 5.

$$(3.1) \quad \varepsilon_v = \varepsilon_1 + 2\varepsilon_3$$

where: ε_v – represents the volumetric strain, ε_1 – represents the axial strain, ε_3 – represents the radial strain.

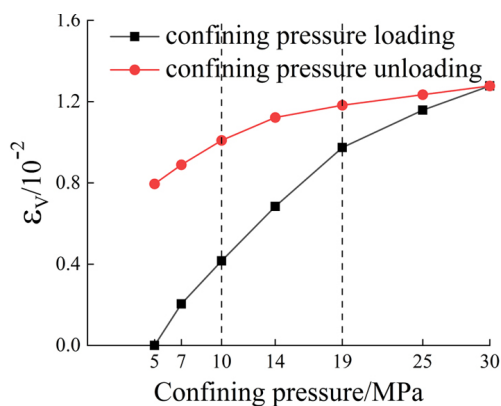


Fig. 5. Strain variation curve with confining pressure

From Fig. 5, it is evident that as the confining pressure gradually increases from 5 MPa to 30 MPa, the volumetric strain exhibits an increasing trend. However, as the confining pressure value progressively rises, the magnitude of volumetric strain growth gradually diminishes. The deformation characteristics can be roughly divided into three stages: During the confining

pressure increase from 5 MPa to 10 MPa, internal microcracks and pores within the specimen are compressed, leading to increased deformation. At this stage, the volumetric compressibility modulus is relatively low, indicating that the specimen is in the plastic deformation stage. Deformation primarily arises from pore closure, and this closure significantly contributes to the substantial reduction in permeability. When the confining pressure ranges from 10 MPa to 19 MPa, the deformation begins to decrease, and the volumetric compressibility modulus slightly increases compared to the previous stage. This indicates that the specimen has entered the linear elastic stage. The deformation primarily results from the compression of the solid-phase framework of the specimen. As the confining pressure rises from 19 MPa to 30 MPa, the slope of the curve significantly decreases, signifying that the compression of internal pores in the specimen has almost reached its limit. At this stage, deformation is minimal, and the volumetric compressibility modulus is at its maximum. The specimen is approaching a critical state, and further deformation becomes challenging due to the inability to further reduce pore size. Therefore, at a macroscopic level, the permeability hardly changes as the confining pressure continues to increase.

During the confining pressure unloading process, a noticeable lag in deformation is observed, which can be attributed to the viscoelastic behavior of the material. Due to the elastoplastic properties of desulfurized gypsum-based concrete, unloading the confining pressure results in the recovery of previous elastic deformations, leading to a reduction in volumetric strain. However, the plastic deformations induced by confining pressure loading cannot be fully recovered. Consequently, during the confining pressure unloading process, the volumetric strain does not return to its initial value when the corresponding confining pressure was applied. This indicates that even as the confining pressure decreases, the previously compressed seepage channels within the specimen cannot fully recover, resulting in an incomplete restoration of permeability following confining pressure unloading.

3.3. Microscopic testing of desulfurized gypsum-based concrete

The macroscopic performance of the specimens is closely related to their microscopic structure. To gather information about the internal pore structure characteristics and microscopic morphology of desulfurized gypsum-based concrete specimens, nuclear magnetic resonance testing and electron microscopy scanning experiments were conducted.

3.3.1. The results of nuclear magnetic resonance testing

Pore size distribution is a crucial aspect of pore structure analysis. By conducting nuclear magnetic resonance tests on fully saturated modified desulfurized gypsum-based concrete specimens, the pore size distribution curve of the specimens is obtained, as shown in Fig. 6.

From Fig. 6, it is evident that the pore size distribution curve of desulfurized gypsum-based concrete exhibits three peaks labeled as P_1 , P_2 , and P_3 . The P_1 peak, corresponding to the smaller pore sizes, has the highest peak value, followed by P_2 and P_3 , which are notably lower. This indicates that the majority of pores within the desulfurized gypsum-based concrete specimens are micro-pores, with the most significant number of pores having a radius (r) around $10^{-2} \mu\text{m}$. Pores with a radius of approximately $10^1 \mu\text{m}$ are relatively scarce. These findings

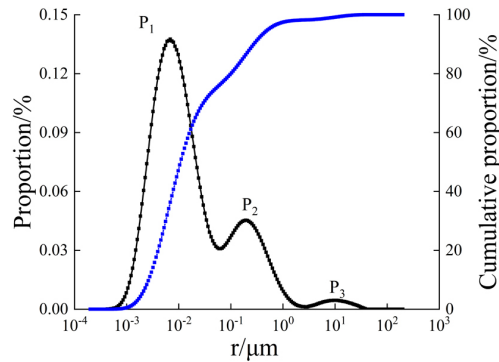


Fig. 6. Pore size distribution and cumulative proportion curve of specimen

suggest that the desulfurized gypsum-based concrete prepared in this study has a dense matrix structure. While larger pores serve as the primary channels for water seepage, their relatively limited presence results in an initial permeability value for the specimens, albeit at a lower magnitude. Furthermore, the application of confining pressure in the experiment compresses these larger pores, leading to an increase in volumetric strain as the confining pressure increases [16]. The microstructural composition of the modified desulfurization gypsum-based concrete, along with its response to external load, dictates the reduced permeability at the macroscopic level. This decrease is approximately 5% lower compared to analogous concretes, resulting in enhanced impermeability characteristics.

3.3.2. The results of electron microscopy scanning

Through electron microscopy scanning, the internal microscopic morphology of desulfurized gypsum-based concrete is depicted in Fig. 7. The modified desulfurized gypsum-based concrete specimens appear relatively dense, containing a multitude of needle- and rod-shaped

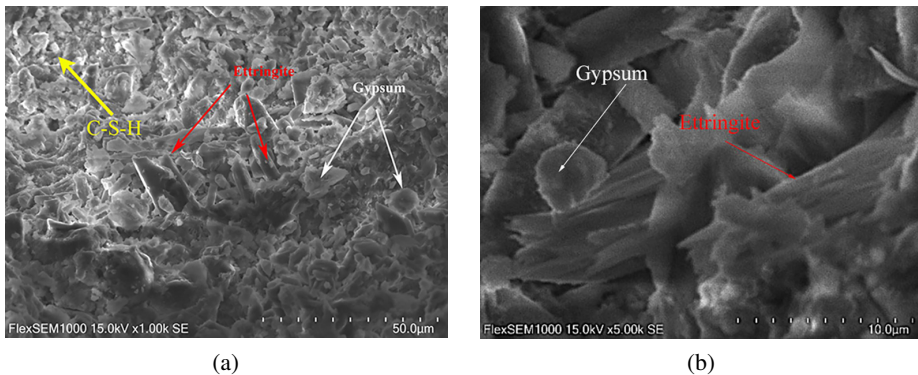


Fig. 7. SEM images of desulfurized gypsum-based concrete: (a) Magnified 1000 times, (b) Magnified 2000 times

AfT crystals. These AfT crystals interconnect with fibrous C–S–H gel, exhibiting an effective particle-to-particle crystal chain filling effect and forming a tightly stable network structure. This enhances the compactness of the matrix, thereby improving the resistance to seepage. Additionally, the C–S–H gel material acts as a protective layer surrounding the hardened particle, contributing to the increased compactness and reduced compressibility of the gypsum composite cementitious material. This neatly explains why modified desulfurized gypsum-based concrete demonstrates an extremely low permeability and exhibits minimal strain values under the influence of confining pressure.

Furthermore, β -type semihydrated gypsum particles are relatively large and transform into short rod-shaped and irregular block-shaped particles during the hydration process, resulting in a larger specific surface area. The addition of aluminum potassium sulfate promotes the growth of long rod-shaped gypsum grains, increasing contact points between them and leading to a denser microstructure. Additionally, the high-efficiency polycarboxylate superplasticizer contains various active groups that facilitate polymerization reactions with the grains, forming stable polymers between them. The comb-shaped adsorption effect of the superplasticizer provides strong electrostatic repulsion between particles and generates steric hindrance on the surface of gypsum particles, enhancing their dispersion stability and water reduction rate. Through the microscopic structure, it is evident that modified desulfurized gypsum-based concrete exhibits high density and excellent impermeability. This significantly increases the potential of using modified desulfurized gypsum as a replacement for cement.

4. Conclusions

1. The permeability of altered desulfurized gypsum-based concrete was assessed at various confining pressures. The imposition of confining pressure results in the compression of internal pores, thereby diminishing permeability. Subsequently, upon the reduction of the confining pressure, the elastic deformation within the specimen rebounded, consequently resulting in an augmentation in permeability.
2. The volumetric strain encountered during the confining pressure triaxial permeation process of modified desulfurized gypsum-based concrete unfolded in three discernible phases: elastic, elastic-plastic, and critical states. The application of confining pressure triggered the compression of the internal structure of the specimens, resulting in an increase in volumetric strain and a simultaneous decrease in permeability due to the constriction of fluidic pathways.
3. The internal pore structure of the altered desulfurization gypsum-based concrete specimens primarily comprised micropores, exhibiting a compact microstructure and minimal permeability at the scale of 10^{-17} m^2 .

Acknowledgements

The underlying project was funded by the Anhui Provincial Natural Science Foundation (2108085ME155).

References

- [1] S. Huang, J.Y. Wang, P. Guo, and Z.N. Li, “Short-term strategy and long-term prospect of energy structure optimization under carbon neutrality target”, *Chemical Industry and Engineering Progress*, vol. 41, no. 11, pp. 5695–5708, 2022, doi: [10.16085/j.issn.1000-6613.2022-1209](https://doi.org/10.16085/j.issn.1000-6613.2022-1209).
- [2] L. Wang, Y. Zhou, Z.P. Chuang, L.C. Chen, and Q.L. Sun, “Study on the strength and carbonation resistance of desulfurized gypsum-based supersulfate cement concrete”, *China Concrete and Cement Products*, no. 3, pp. 85–90, 2022, doi: [10.19761/j.1000-4637.2022.03.085.06](https://doi.org/10.19761/j.1000-4637.2022.03.085.06).
- [3] Y.L. Gao, Z.H. Zhu, H. Meng, X.L. Hu, and Z.K. Li, “Synergistic enhancement mechanism of calcium carbide residue-desulfurization gypsum-steel slag modified geopolymer”, *Journal of Building Materials*, vol. 26, no. 8, pp. 870–878, 2023, doi: [10.3969/j.issn.1007-9629.2023.08.007](https://doi.org/10.3969/j.issn.1007-9629.2023.08.007).
- [4] Z.Y. Liu, W. Ni, Y. Li, H.J. Ba, N. Li, Y.J. Ju, B. Zhao, G.L. Jia, and W.T. Hu, “The mechanism of hydration reaction of granulated blast furnace slag-steel slag-refining slag-desulfurization gypsum-based clinker-free cementitious materials”, *Journal of Building Engineering*, vol. 44, art. no. 103289, 2021, doi: [10.1016/j.job.2021.103289](https://doi.org/10.1016/j.job.2021.103289).
- [5] P. Tan, J.X. Liu, and Z.W. Zhang, “The Research on preparation of binding material and concrete with desulphurization gypsum”, *Multipurpose Utilization of Mineral Resources*, no. 5, pp. 43–46, 2008.
- [6] X. Shi, C.X. Rong, B. Wang, H. Cheng, H.Q. Song, and G.H. Li, “Experimental study on physical and mechanical properties of modified desulfurization gypsum-based concrete”, *Science Technology and Engineering*, vol. 18, no. 21, pp. 288–293, 2018.
- [7] E. Aprianti, “A huge number of artificial waste material can be supplementary cementitious material (SCM) for concrete production—a review part II”, *Journal of Cleaner Production*, vol. 142, pp. 4178–4194, 2017, doi: [10.1016/j.jclepro.2015.12.115](https://doi.org/10.1016/j.jclepro.2015.12.115).
- [8] W.P. Xue, Z.S. Yao, W. Jing, B. Tang, G. Kong, and H. Wu, “Experimental study on permeability evolution during deformation and failure of shaft lining concrete”, *Construction and Building Materials*, vol. 195, pp. 564–573, 2019, doi: [10.1016/j.conbuildmat.2018.11.101](https://doi.org/10.1016/j.conbuildmat.2018.11.101).
- [9] Z.A. Kameche, F. Ghomari, M. Choinska, and A. Khelidj, “Assessment of liquid water and gas permeabilities of partially saturated ordinary concrete”, *Construction and Building Materials*, vol. 65, pp. 551–565, 2014, doi: [10.1016/j.conbuildmat.2014.04.137](https://doi.org/10.1016/j.conbuildmat.2014.04.137).
- [10] Y.Y. Yang, C.B. Jiang, X.W. Guo, S.J. Peng, J.J. Zhao, and F.Z. Yan, “Experimental investigation on the permeability and damage characteristics of raw coal under tiered cyclic unloading and loading confining pressure”, *Powder Technology*, vol. 389, pp. 416–429, 2021, doi: [10.1016/j.powtec.2021.05.062](https://doi.org/10.1016/j.powtec.2021.05.062).
- [11] W.P. Xue, X.Y. Liu, W. Jing, Z.S. Yao, C. Gao, and H.P. Li, “Experimental study and mechanism analysis of permeability sensitivity of mechanically damaged concrete to confining pressure”, *Cement and Concrete Research*, vol. 134, art. no. 106073, 2020, doi: [10.1016/j.cemconres.2020.106073](https://doi.org/10.1016/j.cemconres.2020.106073).
- [12] C.X. Zhao, J.F. Liu, C. Lyu, D. Xu, C. Liang, and Z.C. Li, “Investigation on the mechanical behavior, permeability and failure modes of limestone rock under stress-seepage coupling”, *Engineering Failure Analysis*, vol. 140, art. no. 106544, 2022, doi: [10.1016/j.engfailanal.2022.106544](https://doi.org/10.1016/j.engfailanal.2022.106544).
- [13] H. Yang, S.K. Sinha, Y. Feng, et al., “Energy dissipation analysis of elastic–plastic materials”, *Computer Methods in Applied Mechanics and Engineering*, vol. 331, pp. 309–326, 2018, doi: [10.1016/j.cma.2017.11.009](https://doi.org/10.1016/j.cma.2017.11.009).
- [14] S. Ghabezloo, J. Sulem, S. Guédon, D.B. McCallen, and B. Jeremić, “Effective stress law for the permeability of a limestone”, *International Journal of Rock Mechanics and Mining Sciences*, vol. 46, no. 2, pp. 297–306, 2009, doi: [10.1016/j.ijrmms.2008.05.006](https://doi.org/10.1016/j.ijrmms.2008.05.006).
- [15] F.Q. Wang, W.P. Xue, Z.D. Qiao, W. Jun, and L.W. Jing, “Study on strength characteristics and permeability of chlorite schist during triaxial compression permeability”, *Archives of Civil Engineering*, vol. 69, no. 2, pp. 353–365, 2023, doi: [10.24425/ace.2023.145272](https://doi.org/10.24425/ace.2023.145272).
- [16] N. Nie, “Prediction of concrete life under coupled dry and wet-sulfate erosion based on damage evolution equation”, *Archives of Civil Engineering*, vol. 69, no. 4, pp. 679–692, 2023, doi: [10.24425/ace.2023.147683](https://doi.org/10.24425/ace.2023.147683).

Received: 2023-11-02, Revised: 2024-03-05